Research Square

Preprints are preliminary reports that have not undergone peer review.
They should not be considered conclusive, used to inform clinical practice,
or referenced by the media as validated information.

Observability Core Vector Trajectories for Structural Health Monitoring: From Stable States to Structural Change

Martin Hoffmann

martin.hoffmann1@gmail.com

Independent https://orcid.org/0009-0004-9700-9956

Research Article

Keywords: structural health monitoring, infrastructure observability, Observability Core Vector (OCV), Sentinel-1, OCV trajectories, measurement support, state discrimination

Posted Date: November 6th, 2026

DOI: https://doi.org/10.21203/rs.3.rs-11612080/v1

License: This work is licensed under a Creative Commons Attribution 4.0 International License.
Read Full License

Additional Declarations: The authors declare no competing interests.

Observability Core Vector Trajectories for Structural Health Monitoring: From Stable States to Structural Change

Martin Hoffmann[1*]

[1*]Independent Researcher, Espoo, Finland.

Corresponding author(s). E-mail(s): martin.hoffmann@hpi-alumni.de;

Abstract

What does infrastructure look like to radar as it changes, is repaired, reconstructed, or fails? We extend our infrastructure-observability framework into the temporal domain using the Observability Core Vector (OCV), which combines six Sentinel-1 descriptors of cross-acquisition echo consistency and spatial echo-mask geometry. We examine whether OCV trajectories provide complementary information for structural health monitoring across stable operation, controlled state transitions, reconstruction, repair, major configuration change, and documented failures. Physical processes produce distinct, weak, or absent OCV changes depending on the asset, acquisition geometry, measurement support, and temporal reference. Observable area and fragmentation vary across different physical processes but do not share a common health direction, and apparent long-term evolution can depend on the measurement layer. The cases do not support transferable life-cycle trajectories or a universal failure signature. We use the OCV to characterize temporal change in an asset's radar representation and provide complementary information for infrastructure monitoring. Structural interpretation requires independent measurements or validated physical models.

Keywords: structural health monitoring; infrastructure observability; Observability Core Vector (OCV); Sentinel-1; OCV trajectories; measurement support; state discrimination

1 Introduction

In our previous work [1], we defined infrastructure observability through persistent observation and state discrimination. That framework describes whether infrastructure states can be observed and distinguished, but not how their radar representation evolves over time. Here, we add this temporal perspective by representing the radar-observable state with the Observability Core Vector (OCV) and tracking its evolution over time. We examine stable operation in Espoo, controlled state transitions in LUMO [2, 3] and Bautzen [4], reconstruction in KDLO [5], repair at Werder-Havel, and documented failures including Carola [6], Morandi [7], and CTS [8]. Haltern provides an observation-support sensitivity case. We test whether these physical processes produce recurring OCV trajectories and whether any pattern transfers across assets and observation conditions.

2 Observability Core Vector and Trajectories

2.1 Observability Core Vector

Building on our previous framework, we represent the observable state of an infrastructure asset by the six-dimensional Observability Core Vector:

$$\mathbf{OCV}(t) = \left[\gamma^2(t), P(t), D(t), F(t), A(t), S(t)\right].$$

Figure 1 summarizes how physical asset geometry, acquisition geometry, and the measurement support define this radar representation. Table 1 defines the six dimensions

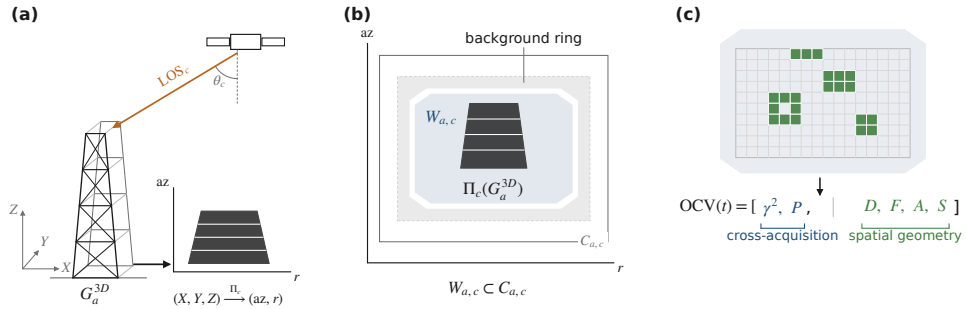


Fig. 1 From physical asset to radar observability. (a) Three-dimensional asset geometry G_a^{3D} under acquisition channel c is projected by Π_c from physical coordinates (X, Y, Z) into native radar coordinates (az, r). (b) The projection defines the asset- and channel-specific measurement support $W_{a,c}$ within the SLC read chip $C_{a,c}$; the surrounding background ring provides local reference statistics without contributing OCV cells. (c) Cross-acquisition measurements and echo-mask geometry within $W_{a,c}$ form the six-dimensional Observability Core Vector $\mathbf{OCV}(t) = [\gamma^2, P, D, F, A, S]$.

and their interpretation. The mask-derived dimensions D, F, A, and S describe related properties of the same echo-mask response and are therefore interpreted jointly

Table 1 Dimensions of the Observability Core Vector (OCV).

Dimension	Name	Description	Interpretation
γ^2	Coherence	Consistency of the radar response across acquisitions	Echo consistency
P	Persistence	Fraction of observations with a valid echo	Observation continuity
D	Density	Fraction of the observation region occupied by echo-mask pixels	Spatial concentration
F	Fragmentation	Number of connected components in the echo mask	Spatial organization
A	Area	Spatial extent of the echo mask	Observable extent
S	Shift	Displacement of the echo mask relative to a reference position	Spatial displacement

rather than as independent evidence. As expressed in Eq. 1, physical changes can alter geometry, orientation, interfaces, and other electromagnetic scattering conditions. These changes modify the complex radar response and can therefore alter the OCV. In simplified form,

$$\Delta X_{\text{physical}} \rightarrow \Delta \mathcal{S} \rightarrow \Delta z \rightarrow \Delta \mathbf{OCV}, \tag{1}$$

where $\mathcal{S}$ denotes the scattering configuration and z the complex SLC response. We therefore interpret OCV change as a change in the radar representation rather than as a direct measurement of the underlying physical process.

2.2 Observability Core Vector Trajectories

We define an OCV trajectory as the temporal evolution of the vector over successive observations:

$$\mathcal{T}_{\text{OCV}} = \{\mathbf{OCV}(t_1), \mathbf{OCV}(t_2), \ldots, \mathbf{OCV}(t_n)\}\,.$$

We use $\mathcal{T}_{\text{OCV}}$ to compare observable evolution across documented physical states and processes.

3 Data and Methods

3.1 Infrastructure Asset Portfolio

We analyze assets spanning stable operation, controlled state transitions, reconstruction, repair, failure, and major configuration change. We assign analytical roles from documented physical processes and experimental conditions, independently of the observed OCV (Table 2).

Table 2 Infrastructure asset portfolio and analytical role of each case.

Role	Asset	Asset type	Physical process
Primary	Espoo	Telecommunications mast	Stable operation
Primary	LUMO	Lattice tower	Controlled transition [2, 3]
Primary	Bautzen	Prestressed-concrete bridge	Controlled transition [4]
Primary	KDLO	Tower structure	Reconstruction [5]
Primary	Carola	Bridge	Documented failure [6]
Validation	Werder-Havel	Bridge	Repair intervention
Validation	Morandi	Bridge	Documented failure [7]
Validation	CTS	Building	Progressive failure [8]
Sensitivity	Haltern	Wind turbine	Configuration and support change

3.2 Radar Observation Support

Three-dimensional object models can be related to SAR image geometry to account for radar viewing configuration [9]. Building on our previous framework [1], we replace fixed-size image chips with asset- and channel-specific measurement support derived from projected asset geometry. For each channel c, we project the three-dimensional geometry G_a^{3D} of asset a into native radar coordinates. For asset height h_a, the height-induced shift in slant-range samples is

$$\Delta r_{h,a,c} = \frac{h_a \cos\theta_c}{\Delta r_{\mathrm{slant},c}}.$$

We define

$$W_{a,c} = \mathrm{dilate}\left(\mathrm{Hull}\left[\Pi_c(G_a^{3D})\right], \mathbf{m}_{a,c}\right),$$

where Π_c denotes the channel-specific projection and $\mathbf{m}_{a,c} = (m_{r,a,c}, m_{\mathrm{az},a,c})$ accounts for modeling and relative-registration uncertainty. Only cells within $W_{a,c}$ contribute to threshold estimation, echo-mask extraction, and OCV computation. A rectangular bounding box $C_{a,c}$ provides the native single-look complex (SLC) read chip,

$$W_{a,c} \subseteq C_{a,c},$$

without adding measurement cells. A separate background ring provides local reference statistics and does not contribute to the OCV. Figure 2 illustrates the distinction between data access, measurement support, and echo-mask extraction. We calculate ground-range spacing as

$$\Delta r_{\mathrm{ground},c} = \frac{\Delta r_{\mathrm{slant},c}}{\sin\theta_c}.$$

We retain only tracks with complete measurement support throughout the analysis period. For Espoo, this leaves one ASC and one DESC relative orbit.

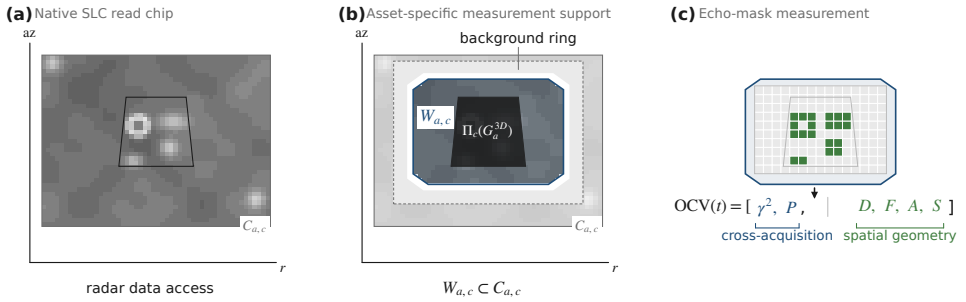


Fig. 2 From radar data to OCV measurement. (a) The native SLC read chip $C_{a,c}$ provides the radar data for asset a and acquisition channel c. (b) Projected asset geometry $\Pi_c(G_a^{3D})$ defines the measurement support $W_{a,c}$ within $C_{a,c}$; the surrounding background ring provides local reference statistics without contributing OCV cells. (c) Echo-mask extraction within $W_{a,c}$ yields the spatial dimensions D, F, A, and S, which combine with the cross-acquisition dimensions γ^2 and P to form $\mathbf{OCV}(t) = [\gamma^2, P, D, F, A, S]$.

3.3 Echo-Mask Extraction

We extract each echo mask from $W_{a,c}$ using native SLC intensity. The background ring provides local reference statistics but does not contribute to the OCV. We retain observations below the minimum mask requirements as missing rather than assigning zero.

3.4 OCV Computation

For each valid acquisition, we compute

$$\mathbf{OCV}_{a,c}(t) = \left[\gamma^2(t), P(t), D(t), F(t), A(t), S(t)\right].$$

We derive A, D, F, and S from the echo mask; γ^2 characterizes cross-acquisition consistency and P observation persistence. We keep ASC and DESC channels separate.

3.5 Temporal and Cross-Asset Analysis

We compare OCV trajectories with independently documented states and events while keeping acquisition channels separate. For labeled states, we use the State Discrimination Score (SDS) introduced previously [1].

Temporal trends.

For continuous trajectories and pre-event periods, we estimate Theil–Sen slopes [10] with 95% moving-block bootstrap confidence intervals. We consider a trend supported only when its interval excludes zero.

Measurement-layer sensitivity.

Where multiple committed measurement layers exist, we analyze each separately. Layer-specific disagreement indicates dependence on the observation definition.

OCV reconfiguration.

For each positive-valued dimension $x \in \{\gamma^2, P, A, D, F\}$, we compute

$$r_x(t) = \text{median}[\log x(t)] - \text{median}[\log x_{\text{ref}}],$$

and

$$z_x(t) = \frac{r_x(t)}{\text{MAD}[\log x_{\text{ref}}]}.$$

We retain S on its native scale and standardize it analogously. For (γ^2, P), we define

$$R_B(t) = \sqrt{\frac{z_{\gamma^2}(t)^2 + z_P(t)^2}{2}},$$

and for (A, D, F, S),

$$R_G(t) = \sqrt{\frac{z_A(t)^2 + z_D(t)^2 + z_F(t)^2 + z_S(t)^2}{4}}.$$

R_B and R_G quantify direction-independent departure; the signed z_x components retain direction. We interpret all quantities within their asset- and channel-specific reference distributions. For monthly analyses, we define the reference envelope from the 5th–95th percentiles of monthly reference values aggregated at the same temporal resolution. Vertical shading denotes the reference period and horizontal shading its empirical envelope. Meteorological variables provide context only.

Acquisition geometry.

For Carola, we analyze the ASC incidence-angle clusters at 36.9° and 44.8° and the DESC track separately.

Post-event decomposition.

For failure cases, area-free models describe total change and area-adjusted models test residual differences at comparable A. We assess robustness using block-bootstrap intervals, multiple-testing correction, common support, and size-matched pre-event placebos where the record permits.

Paired control.

For Bautzen, we analyze paired bridge–control differences for each acquisition because structural-state periods coincide with the measurement campaigns.

4 Results

4.1 Primary OCV Trajectories

4.1.1 Stable Reference: Espoo

Espoo shows no supported long-term trend in any OCV dimension on either retained track. Absolute levels differ between ASC and DESC, so temporal stability applies within acquisition geometry rather than across tracks.

4.1.2 Controlled State Transitions: LUMO and Bautzen

LUMO and Bautzen provide independently defined structural states but different OCV changes. We therefore compare state discrimination by dimension and acquisition channel. The complete OCV trajectories for both cases are shown in Figs. A1 and A2. For LUMO, discrimination depends on dimension, channel, and damage state

Table 3 Maximum pairwise State Discrimination Scores for selected LUMO OCV dimensions. The confidence interval refers to Cliff's δ for the winning state pair.

Channel	Dimension	SDS	δ	CI lower	CI upper	n_1/n_2
ASC	F	7.12	−0.713	−0.950	−0.406	40/4*
ASC	A	5.94	−0.594	−0.963	−0.100	40/4*
ASC	γ^2	4.88	+0.487	−0.013	+0.900	40/4*
ASC	P	4.69	−0.469	−0.744	−0.150	40/8
ASC	D	3.35	+0.335	−0.135	+0.760	40/5
DESC	D	3.66	+0.366	+0.104	+0.602	81/11
DESC	F	3.08	−0.308	−0.543	−0.043	81/11
DESC	γ^2	2.88	+0.288	−0.071	+0.623	81/11

*The damaged-state sample contains fewer than five observations. The winning pairs are Healthy–DAM6 for ASC F, A, and γ^2; Healthy–DAM3 for ASC P; and Healthy–DAM4 for ASC D and all reported DESC dimensions.

(Table 3). ASC P provides the strongest well-supported separation ($SDS = 4.69$, $\delta = -0.469$). Higher scores for ASC F and A under DAM6 rely on only four damaged observations; DESC D and F also separate states. Several dimensions reach the previously reported H2 damping benchmark [1]. Unpaired Bautzen discrimination remains weak, with all bootstrap intervals including zero (Table 4). The paired bridge–control analysis changes this result: A increases by a factor of 1.51 from RS to DS1 and 1.96 from RS to DS2. Corrected RS–DS2 differences also occur in D and F, whereas S, P, and γ^2 remain weaker after multiplicity correction.

Controlled-State Comparison

We find that LUMO distinguishes structural configurations, but its OCV departure does not follow the measured modal-frequency change. Bautzen's point estimates

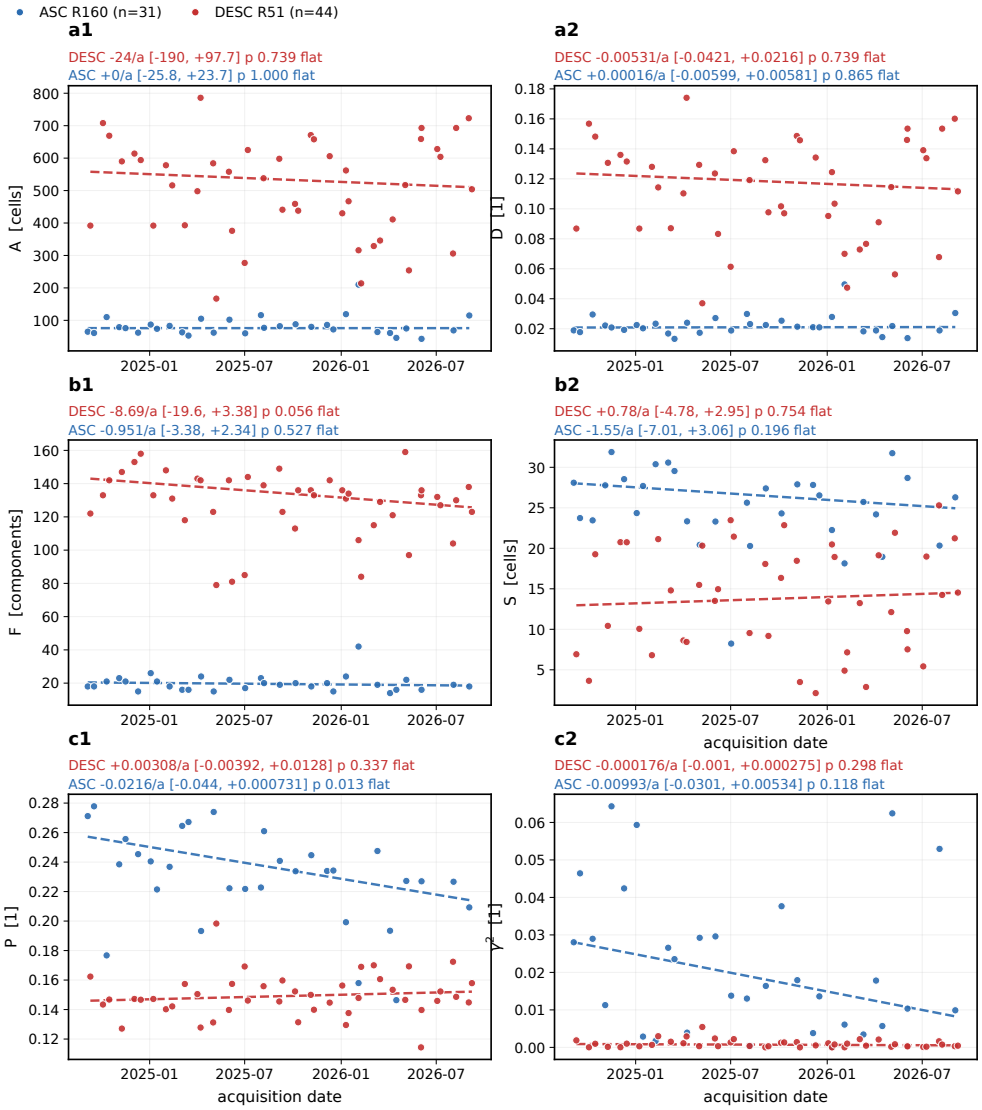


Fig. 3 Two-year OCV trajectories for the Espoo stable-reference asset. ASC and DESC acquisition tracks are shown separately; Theil–Sen slopes and 95% moving-block bootstrap confidence intervals quantify long-term drift.

increase across states, although limited end-state samples leave this progression unresolved. Both cases show reconfiguration in DESC γ^2 and P, while their spatial responses differ (Fig. 4).

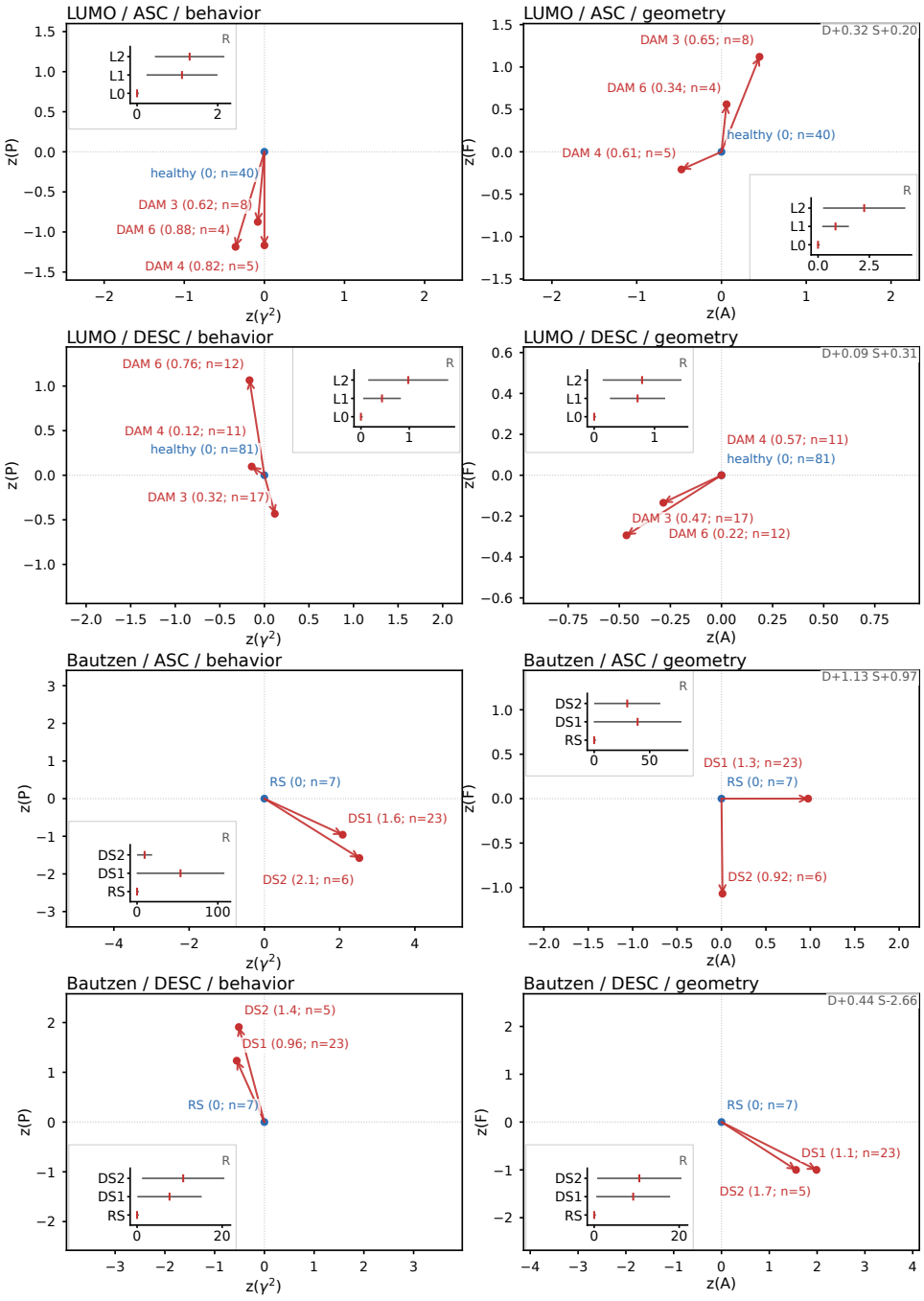


Fig. 4 OCV reconfiguration across the controlled LUMO and Bautzen states. Each asset is standardized against its own reference, so values are not compared directly between assets. The cross-acquisition block comprises γ^2 and P; the spatial block comprises A, D, F, and S, with A and F shown in projection. Arrows indicate reference-to-state changes, and insets show R with 95% moving-block bootstrap intervals.

Table 4 Maximum pairwise State Discrimination Scores for selected Bautzen OCV dimensions. All bootstrap intervals include zero.

Channel	Dimension	SDS	δ	CI lower	CI upper	n_1/n_2
DESC	A	3.57	+0.357	−0.100	+0.757	14/10
DESC	P	2.29	−0.229	−0.657	+0.243	14/10
DESC	D	2.14	+0.214	−0.257	+0.671	14/10
DESC	F	2.14	+0.214	−0.257	+0.671	14/10
DESC	S	2.00	+0.200	−0.272	+0.629	14/10
ASC	F	2.02	−0.202	−0.497	+0.102	14/46

The winning pair is RS–DS2 for all reported DESC dimensions and RS–DS1 for ASC fragmentation.

4.1.3 Observability-Regime Change During Reconstruction: KDLO

KDLO shows pronounced multidimensional change during reconstruction (Fig. 5). P changes most strongly among the cross-acquisition dimensions, while A, F, and S drive the spatial departure. We find that the rebuild observations occupy a distinct OCV region rather than returning to the earlier reference state.

4.1.4 Documented Failure: Carola

During the held-out pre-event period, γ^2 increases while P decreases, but R_B does not exceed the empirical monthly reference envelope (Fig. 6). After the collapse, A and F decrease jointly. At comparable A, most differences in γ^2, D, F, and S attenuate; reduced DESC P does not survive multiplicity correction.

4.2 Cross-Asset Validation

4.2.1 Repair and Intervention: Werder-Havel

At Werder-Havel, A and F increase jointly during repair, accompanied by higher R_G, while changes in γ^2 and P remain smaller (Fig. 7). We therefore find pronounced OCV change during a planned intervention, without an inherent health direction.

4.2.2 Documented Failure: Morandi

Morandi shows stronger pre-collapse spatial evolution than Carola, particularly through coupled increases in A and F (Fig. A3). γ^2 and P also change but do not follow a monotonic trajectory toward collapse. After adjustment for A, D retains the only difference satisfying the complete robustness criteria. The limited post-collapse sample constrains interpretation of the remaining dimensions.

4.2.3 Progressive Failure Process: CTS

CTS shows substantial pre-event variability without a uniform progressive OCV trajectory (Fig. A4). On the preregistered support-sized series, we resolve no long-term γ^2 trend (0.000167 $\gamma^2\,\mathrm{yr}^{-1}$; 95% CI: −0.000813 to 0.001562). A negative trend appears

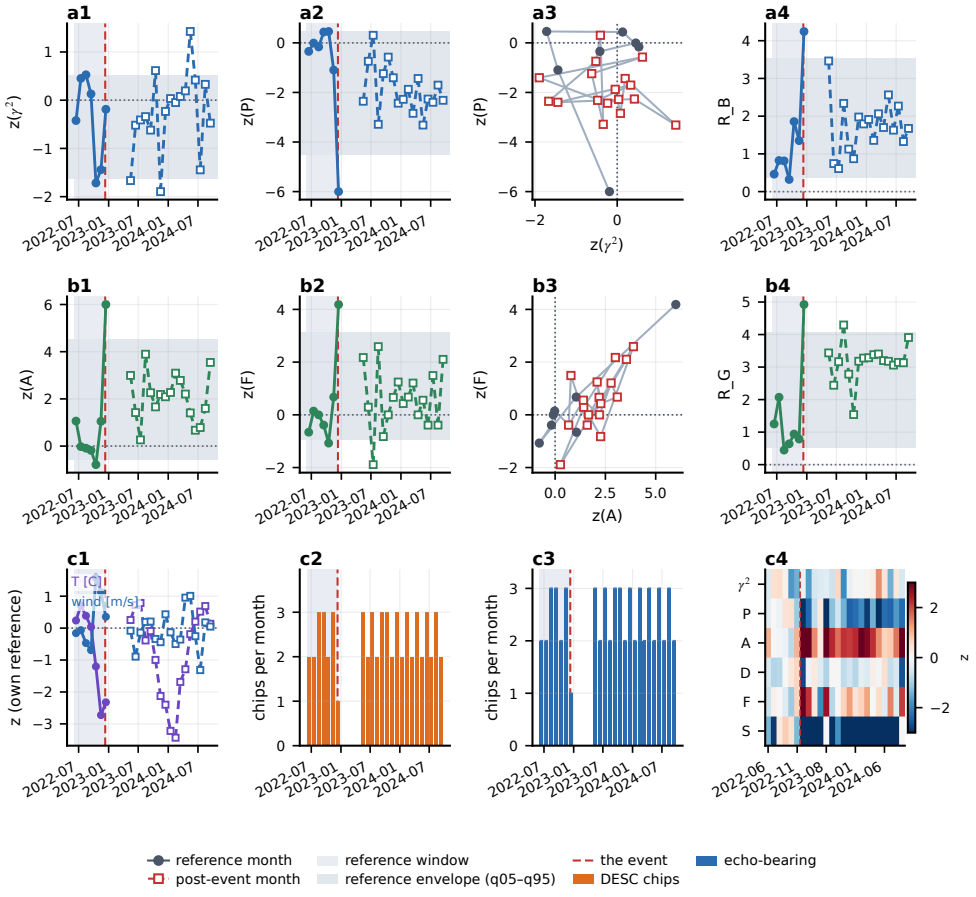


Fig. 5 Monthly OCV trajectory for KDLO before structural loss and during reconstruction. Vertical shading marks the frozen pre-event reference; horizontal shading shows its monthly 5th–95th percentile envelope. Post-event observations represent the rebuild period. The cross-acquisition plane combines γ^2 and P, while the spatial plane shows the A–F projection; D and S remain included in R_G.

on an alternative echo-mask-chip layer but does not reproduce on the primary series or the declared fixed-mask layer. We therefore treat the inferred long-term coherence evolution as measurement-layer dependent.

4.3 Sensitivity and Robustness

4.3.1 Observation-Support Sensitivity: Haltern

At Haltern, A, F, and R_G increase toward the documented transition from an upright to a horizontal configuration, while R_B shows no comparable progression (Fig. A5).

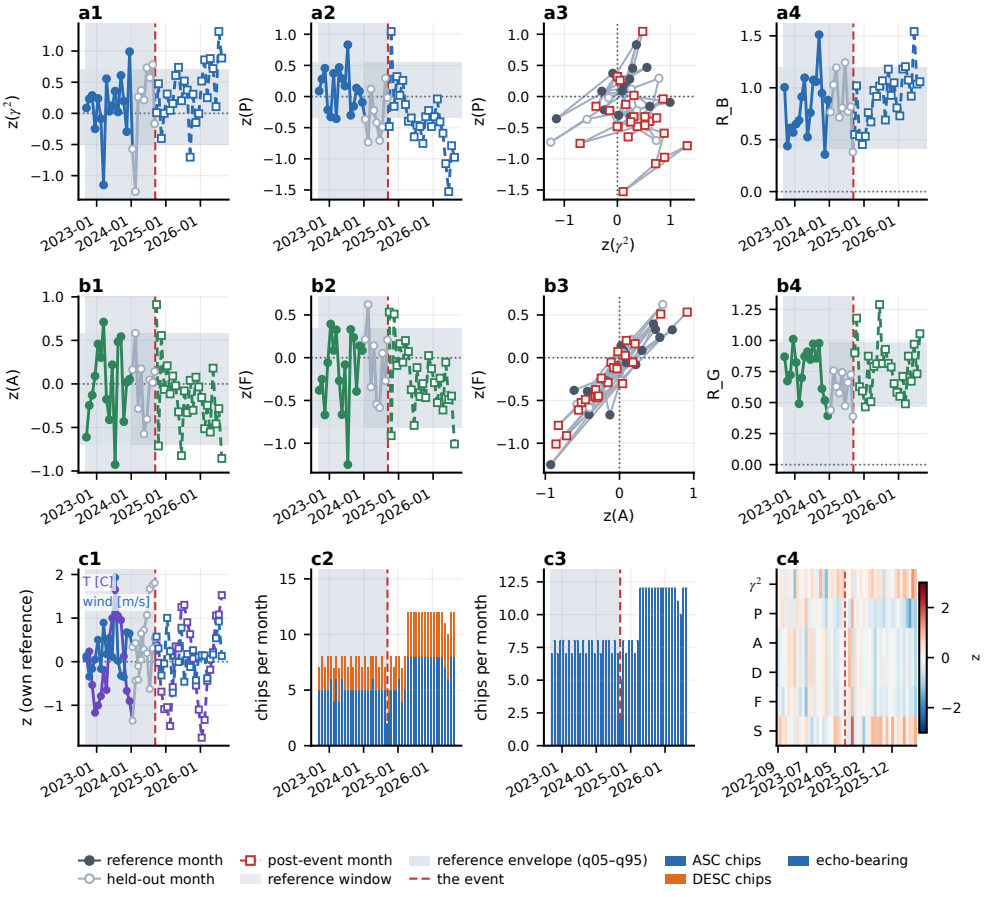


Fig. 6 Monthly OCV trajectory for the Carola bridge relative to the frozen pre-event reference. Vertical shading marks the reference period; horizontal shading shows its monthly 5th–95th percentile envelope. Held-out pre-event observations do not contribute to the reference statistics. The documented collapse separates the pre- and post-event trajectories. The cross-acquisition plane combines γ^2 and P, while the spatial plane shows the A–F projection; D and S remain included in R_G.

The case shows that major morphological change alters the radar representation and that the inferred change depends on the defined measurement support.

4.4 Cross-Asset OCV Trajectory Patterns

Table 5 summarizes the dominant patterns. Across cases, we find strong co-variation between A and F without a common health direction. Both increase during Werder-Havel repair and parts of the Morandi pre-collapse record, yet decrease after the Carola collapse. The failure trajectories also differ temporally. Carola shows held-out change in γ^2 and P, Morandi stronger pre-collapse spatial evolution, and CTS broad variability without a supported long-term coherence trend on the primary measurement

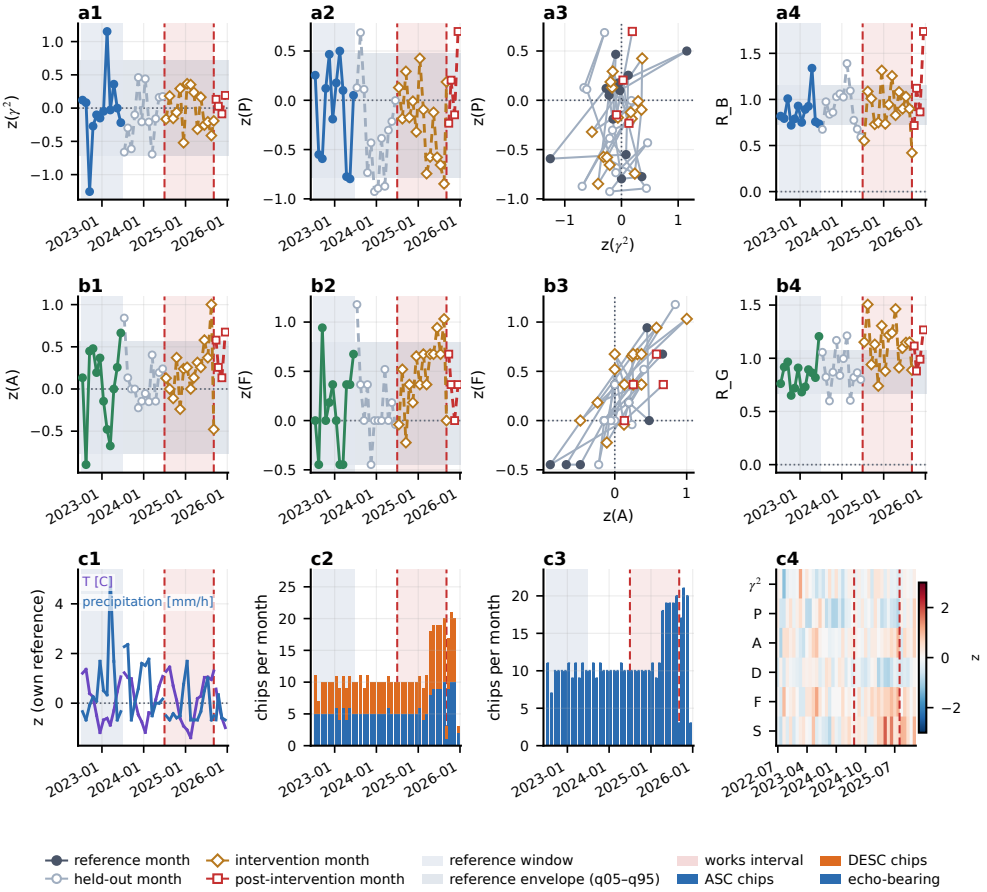


Fig. 7 Monthly OCV trajectory for the Werder-Havel bridge across the documented repair intervention. Vertical shading identifies the frozen pre-intervention reference and intervention period; horizontal shading shows the monthly 5th–95th percentile reference envelope. The cross-acquisition block contains γ^2 and P, while the spatial block contains A, D, F, and S.

layer. We therefore find no common approach-to-failure trajectory. After adjustment for A, most post-event differences attenuate. Morandi D is the only residual finding that satisfies the complete robustness criteria (ratio 0.31, 95% CI: 0.22–0.52).

5 Discussion

5.1 Observable Change Across Physical Processes

We find that neither direction nor size of OCV change transfers consistently across physical processes. Controlled state changes, reconstruction, repair, and failure can all move an asset away from its earlier radar representation, but they do so through different dimensions and directions. This result separates OCV change from structural

Table 5 Recurring and case-specific OCV trajectory patterns.

OCV pattern	Cases	Interpretation
Stable within acquisition geometry	Espoo	Bounded variation without a supported long-term trend.
State-specific change	LUMO, Bautzen	Dimension- and channel-specific differences across independently defined states.
Reconstruction-associated regime change	KDLO	Persistent multidimensional departure during reconstruction.
Intervention-associated change	Werder-Havel	Predominantly spatial change during repair without an implied health direction.
Failure-associated change	Carola, Morandi, CTS	Asset-specific temporal patterns without a common complete-vector trajectory.
Morphology- and support-sensitive change	Haltern	Spatial change whose interpretation depends on asset configuration and measurement support.

health. In particular, Werder-Havel and KDLO show that substantial departures also accompany planned intervention and reconstruction. We therefore interpret OCV trajectories as changes in radar observability rather than movement along a universal deterioration axis.

5.2 No Universal Failure Signature

Carola, Morandi, and CTS show different temporal organizations of pre- and post-event change. Carola exhibits held-out change in γ^2 and P followed by a clearer post-collapse spatial reduction; Morandi shows stronger pre-collapse spatial evolution; CTS shows substantial variability without a supported long-term coherence trend on the primary measurement layer. These differences do not support a universal failure signature, common precursor trajectory, or fixed cross-asset threshold.

5.3 Measurement Dependence and Comparability

Observation geometry, measurement support, reference definition, and measurement layer constrain valid comparison. CTS demonstrates layer dependence directly: a negative coherence trend appears on an alternative echo-mask chip but not on the preregistered support-sized series. Haltern shows support dependence during a major change in asset morphology. We therefore compare OCV quantities within fixed asset- and channel-specific observation definitions rather than against universal thresholds. Meteorological variables provide contextual information but do not enter the OCV or R_B/R_G.

5.4 From Observability Change to Evidence

The OCV characterizes how an asset appears to radar; it does not establish the physical origin of change. This distinction is particularly important for A, D, F, and S, which describe related properties of the same echo mask rather than four independent evidence channels. Physical interpretation therefore requires complementary measurements or validated models. We retain the OCV as a representation of radar observability rather than a direct measure of structural condition.

5.5 Limitations and Outlook

Unequal temporal coverage, limited post-event samples, environmental variability, acquisition geometry, measurement support, and reference definition constrain cross-case comparison. CTS additionally shows that temporal inference can depend on the measurement layer. Future work should compare OCV trajectories with complementary physical measurements and validated models while keeping these evidence streams distinct. This provides a path from describing observable change towards testing its physical origin.

6 Conclusion

The OCV extends our infrastructure-observability framework into the temporal domain by representing how an asset's radar-observable state evolves over time. Stable operation, controlled state changes, reconstruction, repair, major configuration change, and documented failure produce distinct trajectories, but no transferable life-cycle trajectory or universal failure signature. Cross-acquisition and spatial information are complementary, yet their direction carries no universal health meaning. A and F, for example, increase during repair and parts of Morandi's pre-collapse evolution but decrease after the Carola collapse. CTS further shows that inferred long-term coherence evolution can depend on the measurement layer. The OCV characterizes change in an asset's radar representation rather than structural condition itself. Establishing the physical origin and relevance of that change requires complementary measurements or validated physical models.

Acknowledgements. The author appreciates the support and patience of his family, whose understanding made this work possible.

Declarations

Funding. The author received no funding for this work.

Competing interests. The author declares no competing interests.

Ethics approval and consent to participate. Not applicable.

Consent for publication. Not applicable.

Data availability. The processed Sentinel-1 feature tables, OCV results, and analysis materials required to reproduce the reported results are publicly available through the associated Zenodo repository [11]. Sentinel-1 SLC data are available separately through the Copernicus Data Space Ecosystem. External benchmark and case-study data remain subject to their original sources and licenses. LUMO benchmark data and modal information are documented in the published LUMO studies [2, 3], while the Bautzen openLAB reference data are described by [4].

Materials availability. Not applicable.

Code availability. The code used to calculate the OCV trajectories and generate the figures presented in this study is publicly available on GitHub and archived in Zenodo at https://doi.org/10.5281/zenodo.23915367.

Author contributions. Martin Hoffmann: Conceptualization, methodology, software, formal analysis, investigation, visualization, and writing–original draft.

Appendix A Complete Case Trajectories

This appendix presents the complete OCV trajectories for the controlled-state, validation, and sensitivity cases whose principal quantitative findings are reported in the main text. All figures use the visual conventions defined in Section 3. Vertical shading identifies the frozen reference period, and horizontal shading shows the corresponding monthly 5th–95th percentile reference envelope where applicable.

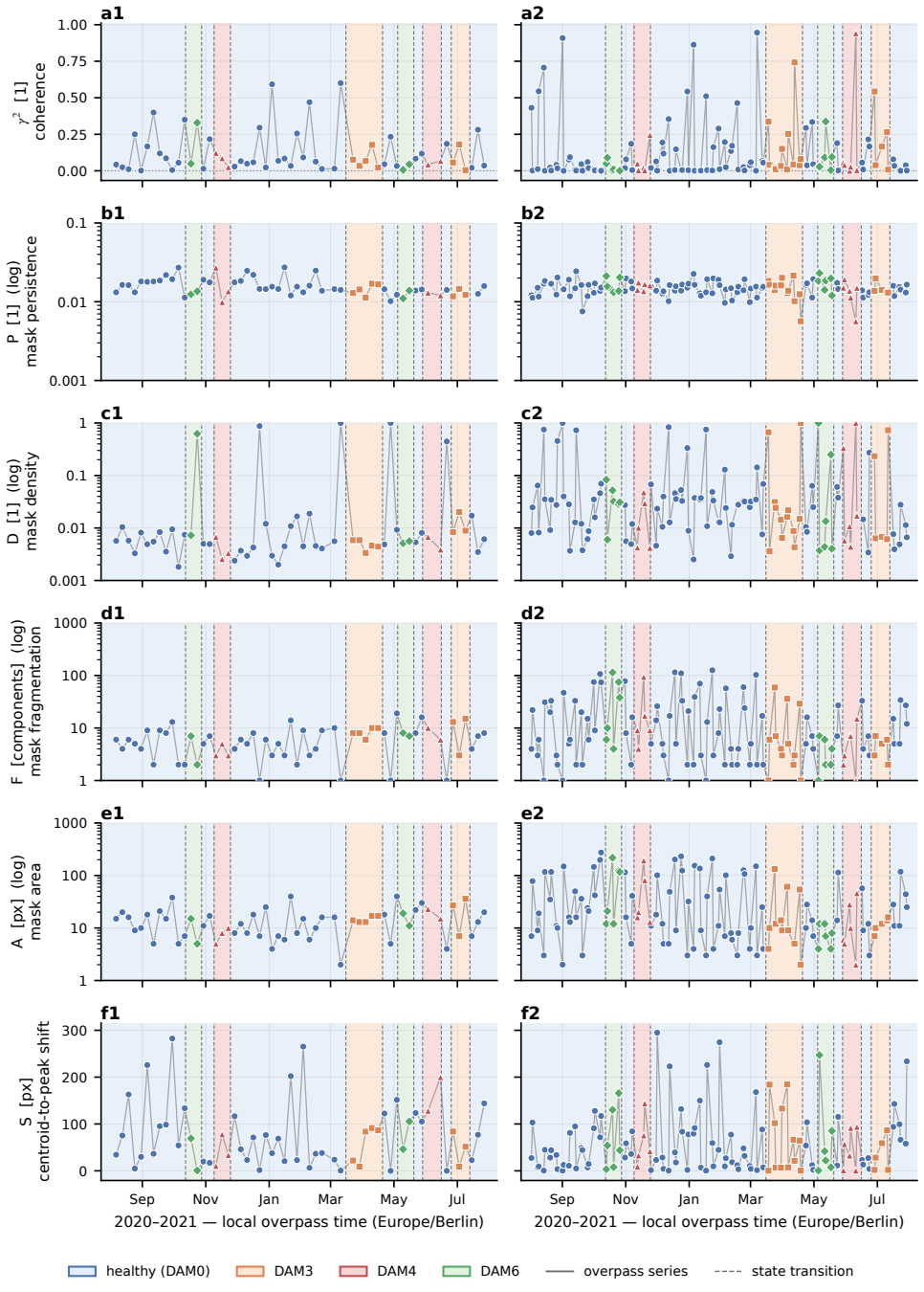


Fig. A1 Complete OCV trajectories for the LUMO lattice tower under the documented Healthy, DAM3, DAM4, and DAM6 states. ASC and DESC acquisition channels are shown separately.

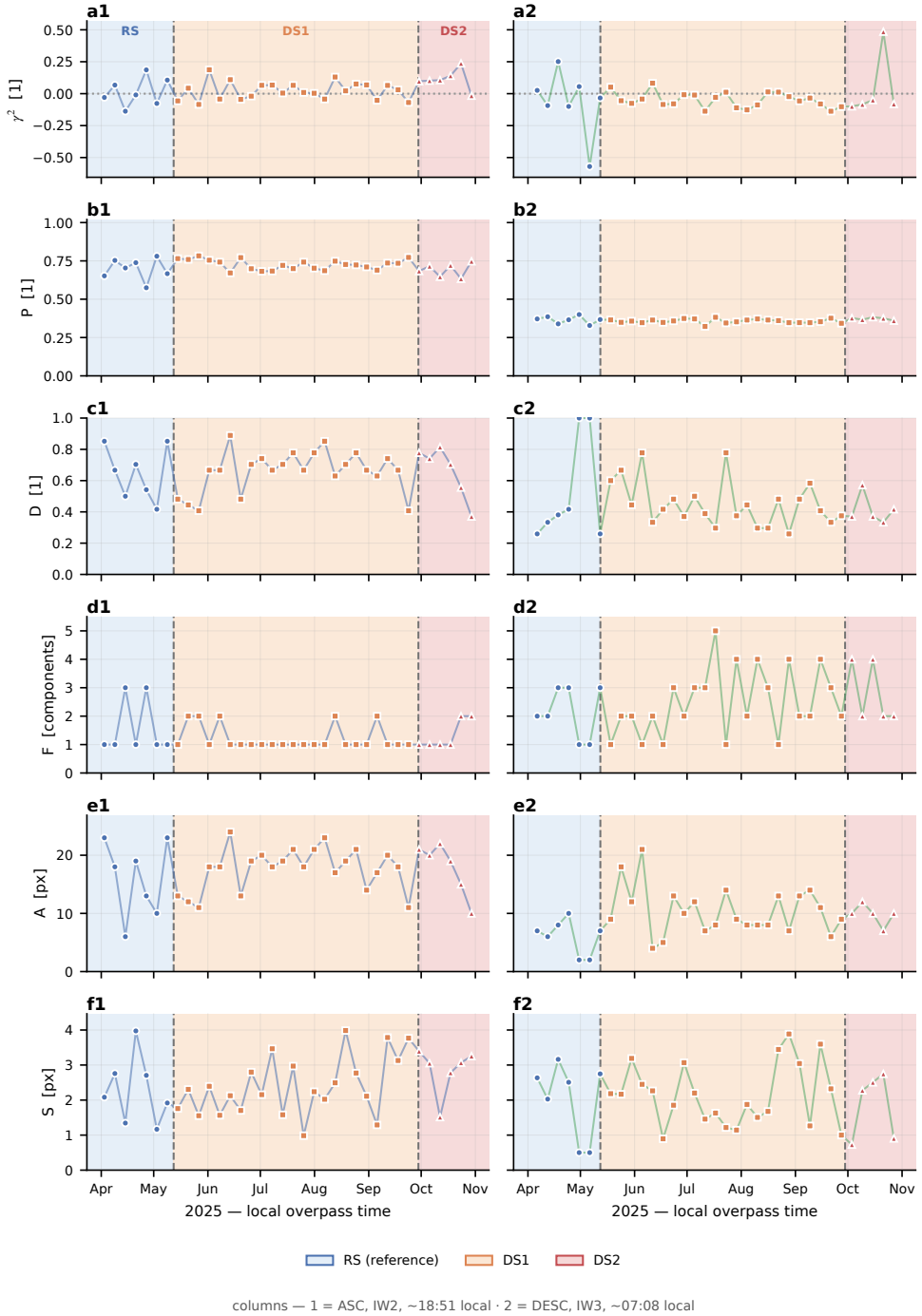


Fig. A2 Complete OCV trajectories for the Bautzen openLAB bridge across the documented RS, DS1, and DS2 states. ASC and DESC acquisition channels are shown separately.

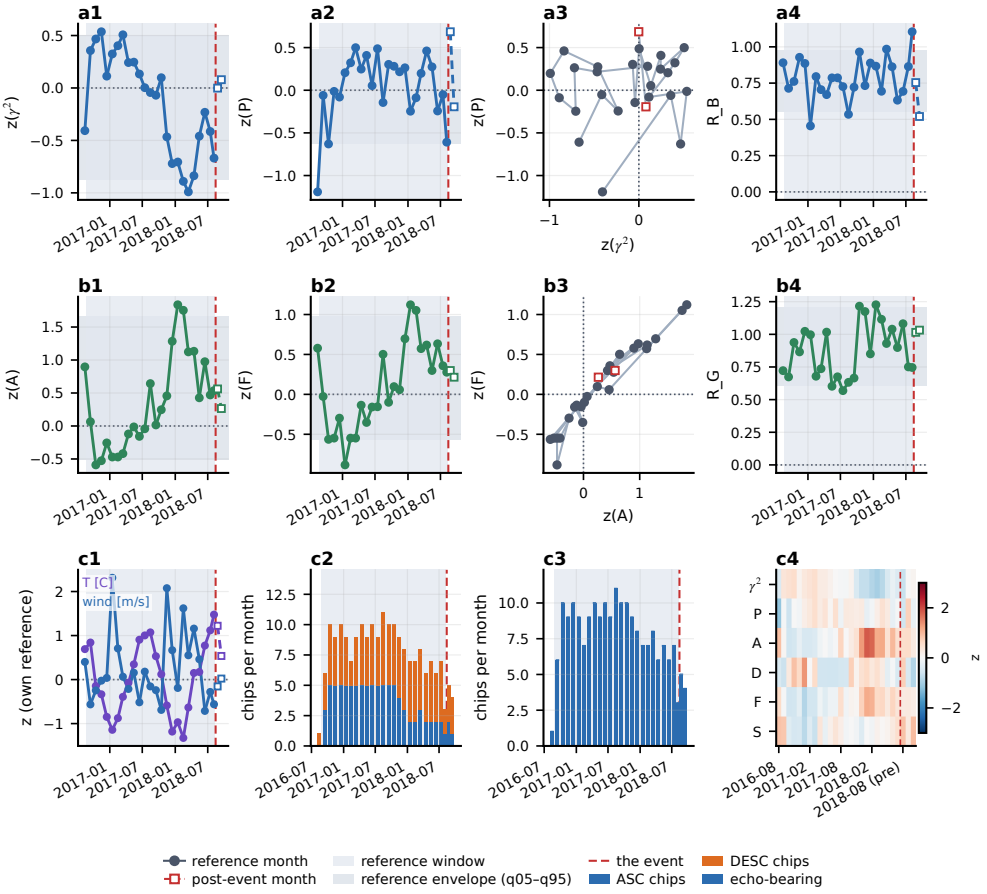


Fig. A3 Monthly OCV trajectory for the Morandi bridge relative to the complete pre-collapse reference regime. Because the pre-collapse observations contribute to their own reference statistics, the figure provides a descriptive temporal analysis rather than a pseudo-prospective anomaly test. The limited post-collapse sample constrains inference about the post-event regime.

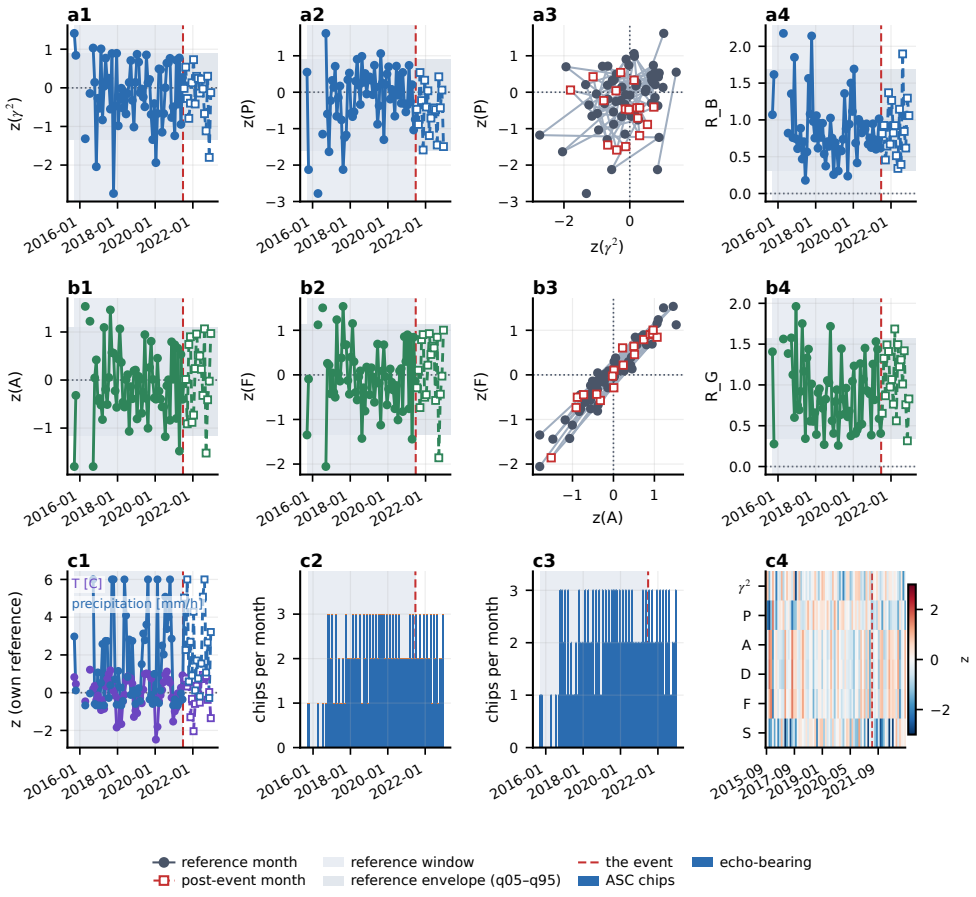


Fig. A4 Monthly OCV trajectory for Champlain Towers South relative to the complete pre-event reference regime. Because the complete pre-event record contributes to the reference statistics, the figure describes temporal evolution rather than a pseudo-prospective precursor test.

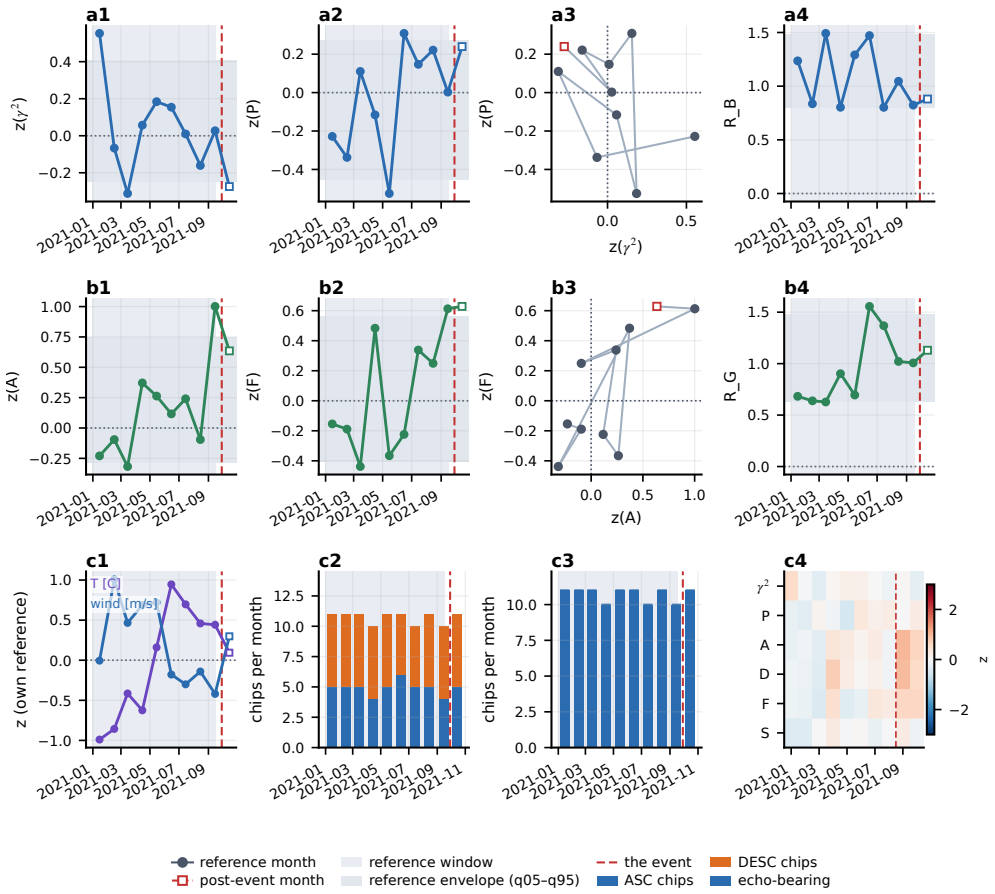


Fig. A5 Monthly OCV trajectory for the Haltern AV9 wind turbine around the documented transition from an upright to a horizontal configuration. The case tests sensitivity to asset morphology and the observation-support definition rather than a transferable failure trajectory.

References

[1] Hoffmann, M.: Observability in infrastructure monitoring: State discrimination and persistent observation from the lumo and espoo case studies. SSRN Electronic Journal (2026) https://doi.org/10.2139/ssrn.7552882

[2] Wernitz, S., Hofmeister, B., Jonscher, C., Griessmann, T., Rolfes, R.: A new open-database benchmark structure for vibration-based structural health monitoring. Structural Control and Health Monitoring **29**(11), 3077 (2022) https://doi.org/10.1002/stc.3077

[3] Römgens, N., Abbassi, A., Jonscher, C., Grießmann, T., Rolfes, R.: On using autoencoders with non-standardized time series data for damage localization. Engineering Structures **303**, 117570 (2024) https://doi.org/10.1016/j.engstruct.2024.117570

[4] Jansen, A., Herbers, M., Richter, B., Walker, M., Jesse, F., Marx, S.: Monitoring data of the openlab research bridge – part 1: Reference condition. Data in Brief **60**, 111624 (2025) https://doi.org/10.1016/j.dib.2025.111624

[5] Mulherin, N.D.: Atmospheric icing and tower collapse in the united states. In: Proceedings of the 7th International Workshop on Atmospheric Icing of Structures (IWAIS'96), Chicoutimi, Quebec, Canada (1996). Presents a database of icing-related communication tower failures in the United States

[6] Marx, S., Scheerer, S., Schacht, G., Fiedler, M., Ritter, R., Clages, L., Voigt, C., Czeschka, D., Ebell, G., Marzahn, G.: Einsturz der carolabrücke in dresden teil 1: Vom ambitionierten entwurf bis zum tragischen teileinsturz. Beton- und Stahlbetonbau **120**(7), 526–536 (2025) https://doi.org/10.1002/best.202500029

[7] Milillo, P., Giardina, G., Perissin, D., Milillo, G., Coletta, A., Terranova, C.: Pre-collapse space geodetic observations of critical infrastructure: The morandi bridge, genoa, italy. Remote Sensing **11**(12), 1403 (2019) https://doi.org/10.3390/rs11121403

[8] National Institute of Standards and Technology (NIST): Technical investigation of the partial collapse of the champlain towers south condominium. Draft/Final Research Report NIST NCSTAR 1, U.S. Department of Commerce, Gaithersburg, MD (2025). https://nist.gov

[9] Auer, S., Bamler, R., Reinartz, P.: RaySAR – 3d SAR simulator: Now open source. In: 2016 IEEE International Geoscience and Remote Sensing Symposium (IGARSS), pp. 6730–6733. IEEE, ??? (2016). https://doi.org/10.1109/IGARSS.2016.7730757

[10] Sen, P.K.: Estimates of the regression coefficient based on kendall's tau. Journal of the American Statistical Association **63**(324), 1379–1389 (1968) https://doi.

org/10.1080/01621459.1968.10480934

[11] Hoffmann, M.: Observability Core Vector Repository. https://doi.org/10.5281/zenodo.23915367